Chinese Chemical Letters 32 (2021) 1191–1196

Contents lists available at ScienceDirect

Chinese Chemical Letters

journal homepage: www.elsevier.com/locate/cclet

Communication

Proton-induced fast preparation of size-controllable MoS_2 nanocatalyst towards highly efficient water electrolysis

Jingjiang Wei, Ge Wang, Yijie Zhang, Shengping Wang, Wanyu Zhao, Qihang Liu, Congcong Liu, Xiaoli Zhao*, Xiaowei Yang*

School of Materials Science and Engineering, Tongji University, Shanghai 201804, China

ARTICLE INFO

Article history:
Received 12 June 2020
Received in revised form 9 July 2020
Accepted 5 August 2020
Available online 7 August 2020

Keywords:
Size-controllable nanocatalys
Proton inducement
MoS_2 nanocatalyst
Hydrogen evolution reaction
Electrode-level performance

ABSTRACT

MoS_2 has emerged for catalyzing the hydrogen evolution reaction. Various notable strategies have been developed to downsize the MoS_2 particles and expose more active edges. However, the restacking issue, which reduces the exposure degree, has rarely been taken into account. Herein, we report on a facile proton-induced fast hydrothermal approach to produce size-controllable MoS_2 nanocatalysts and demonstrate that along the varying of sheet sizes, there is a trade-off between the intrinsic catalytic activity (mainly determined by the unsaturated sulfur on the sheet edges) and the active edge accessibility (influenced by the assembly structure). The size-optimized catalyst delivers a high performance of a low overpotential of ~200 mV at 10 mA/cm^2, a Tafel slope of 46.3 mV/dec, and a stable working state, which is comparable to the recent notable works. Our findings will provide a pathway for its large-scale application and enhance the water electrolysis performance.

Hydrogen, a clean and renewable energy, is one of the most promising alternatives for traditional fossil fuels [1]. Water electrolysis is an ideal approach for hydrogen production, and the key to achieving its practical applications is to develope cost-effective electrocatalyst to accelerate the hydrogen evolution reaction (HER) [2–5]. Pt-based materials possess the best performance in HER, yet their expensiveness and scarcity have hampered the large-scale applications [6–9]. To this end, enormous efforts have been devoted to the non-noble and earth-abundant HER catalysts in the past years [10–15]. Molybdenum disulfide (MoS_2) has drawn great attention due to its low cost and high abundance [16,17]. However, the bulk MoS_2 is not an active HER catalyst because its exposed basal planes are generally inert and the electron/mass transportation is sluggish [18]. Fortunately, both theoretical and experimental studies have verified that the edge sites and defects of MoS_2 are catalytically active owing to the unsaturated sulfur [19–21]. Hence, nanostructured MoS_2 HER catalysts with smaller sheet size and more edge sites exposed are highly desirable in order to realize the superior performance of electrocatalysts. Using ultrasonic exfoliation to cleave bulk MoS_2 into a few nanolayers can increase the exposure of active edge sites; nevertheless, the number of layers and the lateral size of resultant nanosheets are hard to control [22]. Chemical vapor deposition is beneficial for the growth of high-quality MoS_2 nanosheets with controllable sizes, shapes, and structures, but rigorous experimental conditions, such as high vacuum, high temperature, and specific substrates, restricting its wide practical applications [23]. Benefiting from the low-cost precursors (metal salts) and simple manipulation to meet the practical requirements that obtain abundant edge defects [23,24], hydrothermal synthesis of MoS_2 nanosheets has drawn great attention in synthesizing nanostructured MoS_2 electrocatalysts.

Favorable HER performance has been successfully achieved by preparing the defect-rich nanosized MoS_2 flakes with promoted intrinsic catalytic activity [24]. Although the as-prepared MoS_2 nanosheets in the solution can be conveniently stored, separated and easily transferred onto any substrates for electrode construction [23], those MoS_2 nanosheets with exposed edges are easily restacked in the solution because of their high surface energy and interlayer van der Waals attractions. Besides, the aggregate MoS_2 nanoparticles, which greatly impede the ion accessibility of the exposed active sites, reducing the electrocatalytic performance in the electrode level. Therefore, various controllable nanostructures such as hybrid nanoflowers [25,26], hybrid core-shell structure [27,28], nanoconfined structure [29] and vertically aligned nanolayers [30–32] have been reported to design the transport channels with exposed edges by introducing supporters. However, because

* Corresponding authors.
E-mail addresses: zxl36@tongji.edu.cn (X. Zhao), yangxw@tongji.edu.cn (X. Yang).

https://doi.org/10.1016/j.cclet.2020.08.005

of the restacking problem in nanostructured MoS_2 with abundant defects, it remains a great challenge that how to balance the intrinsic catalytic activity (mainly determined by the unsaturated sulfur on the sheet edges) and the active edge accessibility (influenced by the assembly structure) of MoS_2 nanosheets without other dopants to maximize the catalytic performance during electrochemical processes.

Herein, we report a hydrothermal method for the fast synthesis of size-controllable MoS_2 nanocatalysts by pH regulation. We investigated the effects of the acid concentrations on the synthesizing process and the resulting structure of the MoS_2 nanosheets. Results suggested that increasing the proton concentrations can downsize MoS_2 nanosheets with better intrinsic catalytic activity, but lead to serious aggregation of the nanosheets: The increase of proton concentrations may provide more nucleation sites during pretreatment and thus result in the size decrease of the as-formed MoS_2 nanosheets; however, the small size renders the nanosheets freedom to well restack. In other words, our results show that varying the size of the nanosheets, there is a trade-off between the intrinsic catalytic activity and active site accessibility. By the facile pH regulation, the MoS_2 nanosheets with the moderate intrinsic activity and the restacking degree deliver the best catalytic property of ~200 mV at the current density of 10 mA/cm^2, a Tafel slope of 46.3 mV/dec, and long-run stability in our work. Furthermore, MoS_2 nanocatalysts were prepared within 3 h *via* the proton-induced hydrothermal preparation process, leading to significant time savings (the reaction time of recent MoS_2 catalysts prepared by hydrothermal synthesis are shown in Table S1 in Supporting information), which was a benefit for its practical use. Our success in fast synthesis and insights into the edge-exposed MoS_2 catalyst properties provide a simple method to adjust catalytic performance without other dopant and a pathway for the practical applications of non-noble catalysts for water electrolysis.

Sodium molybdate dihydrate ($Na_2MoO_4{\cdot}2H_2O$), sulfuric acid (H_2SO_4), and hydrochloric acid (HCl) were purchased from Sinopharm Chemical Reagent Co., Ltd. Thiourea ($SC(NH_2)_2$) and Nafion solution (5 wt%) were purchased from Sigma-Aldrich.

Typically, 2.5×10^{-3} mol $Na_2MoO_4{\cdot}2H_2O$ and 10×10^{-3} mol $SC(NH_2)_2$ were dissolved in 70 mL HCl solution (pH 1.00, 0.69, 0.50, 0.37 and 0.24). After being stirred to form a homogeneous mixture, the solution was transferred into a 100 mL Teflon-lined stainless-steel autoclave. The autoclave was heated at 200 °C for 3 h and then cooled to room temperature naturally. Thereafter, the products were washed with deionized water assisted by centrifugation for several times to remove redundant HCl and unreacted reagents. The resulting products were collected and maintained in deionized water. The MoS_2 catalyst synthesized with pH 1.00, 0.67, 0.50, 0.37, 0.24 are denoted as MoS_2-1.00, MoS_2-0.67, MoS_2-0.50, MoS_2-0.37, MoS_2-0.24, respectively.

Powder X-ray diffraction (XRD) profiles were recorded on an X-ray diffract meter (D2 PHASER, BRUKER). The scanning electron microscope (SEM) was performed in FEI Nova NanoSEM 450. A JEM-2100 electron microscopy with an accelerating voltage of 200 kV was performed for transmission electron microscope (TEM) measurements. X-ray photoelectron spectroscopy (XPS) measurement was carried out on a Thermo Scientific Escalab 250Xi X-ray photoelectron spectrometer using Al as the exciting source. The dynamic light scattering (DLS) was carried out on Malvern Zetasizer Nano ZS90.

Electrochemical measurements were performed in a three-electrode electrochemical cell with Bio-Logic potentiostat (VMP3). Typically, 1 mL of water-isopropanol solution (volume ratio, 4:1) containing 3 mg MoS_2 catalyst was mixed with 60 μL Nafion by sonicating for 30 min to form a homogeneous ink. Then 5 μL of the ink was dropped onto the glassy carbon electrode with a 3 mm diameter (catalyst loading: 0.21 mg/cm^2). All measurements were performed in the electrolyte of N_2-saturated 0.5 mol/L H_2SO_4 aqueous solution with a graphite rod as the counter electrode, saturated calomel electrode (SCE) as the reference electrode and the glassy carbon electrode loaded with MoS_2 as the working electrode.

The linear sweep voltammetry (LSV) with a scan rate of 5 mV/s and Tafel analysis were conducted for the characterization of HER activity. The double-layer capacitance was measured by cyclic voltammetry (CV) scan with various scan rates (25, 50, 100, 200, 400 mV/s) in the range of 0.25–0.35 V *vs.* SCE. The electrochemical impedance spectroscopy (EIS) measurements were carried out at an overpotential of 250 mV in the frequency range from 10^5 Hz to 0.01 Hz. To investigate the electrochemical stability, chronopotentiometry scan (at 10 mA/cm^2) and CV (−0.3–0.1 V *vs.* RHE at 50 mV/s) were conducted. All data in this work were corrected with iR (removing the effect of solution resistance). All potentials were calibrated to a reversible hydrogen electrode (RHE), E (*vs.* RHE) = E (*vs.* SCE) + 0.241 V.

Proton-induced MoS_2 nanocatalysts were fast prepared by the hydrothermal synthesis from the pre-treatment of precursors ($Na_2MoO_4{\cdot}2H_2O$ and $SC(NH_2)_2$) with the addition of aqueous HCl solution (Fig. S1 in Supporting information). The products MoS_2 powder was characterized by TEM, XRD, and XPS as shown in Fig. S2 (Supporting information), which demonstrate that our fast-prepared material was predominately composed of low-crystalline 2H-MoS_2 nanosheets [31,33]. To investigate the effect of HCl pre-treatment on resultant products and their formed electrode architectures, XRD of the MoS_2 products prepared with various pH was further carried out to analyze the crystalline structure of the synthesized MoS_2 in the assembled electrode. Note that samples for XRD shown in Fig. 1A were prepared from the dried ink for drop-casting to simulate the state of the real electrode, while that for XRD in Fig. S2 was prepared by freeze drying which has an obvious crystal structure. A typical 2H-MoS_2 profile of JCPDS card No. 75-1539 of these samples can be observed [34]. The lower intensity of (100) and (002) peaks indicates a shorter basal plane and less stacking of MoS_2 layers [35]. As seen in Fig. 1B, the intensity of (100) peak decreases along with the decrease of pH. When the pH value decreases to 0.24, the (100) peak even becomes difficult to be observed, which suggests that the lateral size of resultant MoS_2 products was decreased by lowering pH and more edge sites and defects were exposed. Notably, in Fig. 1C, with the decrease of pH, the intensity of (002) peak becomes weaker at first (from pH 1.00 to 0.50) but then becomes stronger (from pH 0.50 to 0.24). The weakening of intensity of the (002) peak is probably due to the proton-induced downsizing of MoS_2 nanosheets at *c* axis. Since the smaller nanosheets with higher surface energy are easier to restack, we could assume that the subsequent increase in (002) peak is mainly attributed to the restacking of further size-decreased MoS_2 nanosheets which decreases the edge-exposing degree [16,36].

To further investigate the pH effect on the size control, SEM was carried out to further investigate the effect of pH on the size of MoS_2 nanosheets as shown in Fig. 1D, which was inconsistent with the results of XRD. Three SEM samples prepared from the ethanol solution of MoS_2 for drop-casting merely shown that the size of resultant MoS_2 products was decreased by lowering pH, which is consistent with the results of DLS (Fig. S3 in Supporting information). Here, we have a clear understanding of the effect of HCl pre-treatment on resultant MoS_2 by summarizing those characterizations. Decreasing the pH value is propitious to decrease the lateral size and thickness of resultant MoS_2 nanosheets. However, the too small MoS_2 nanosheets would tend to restack and aggregate after being assembled into the electrode. Meanwhile, the size decrease is beneficial for the enhancement of

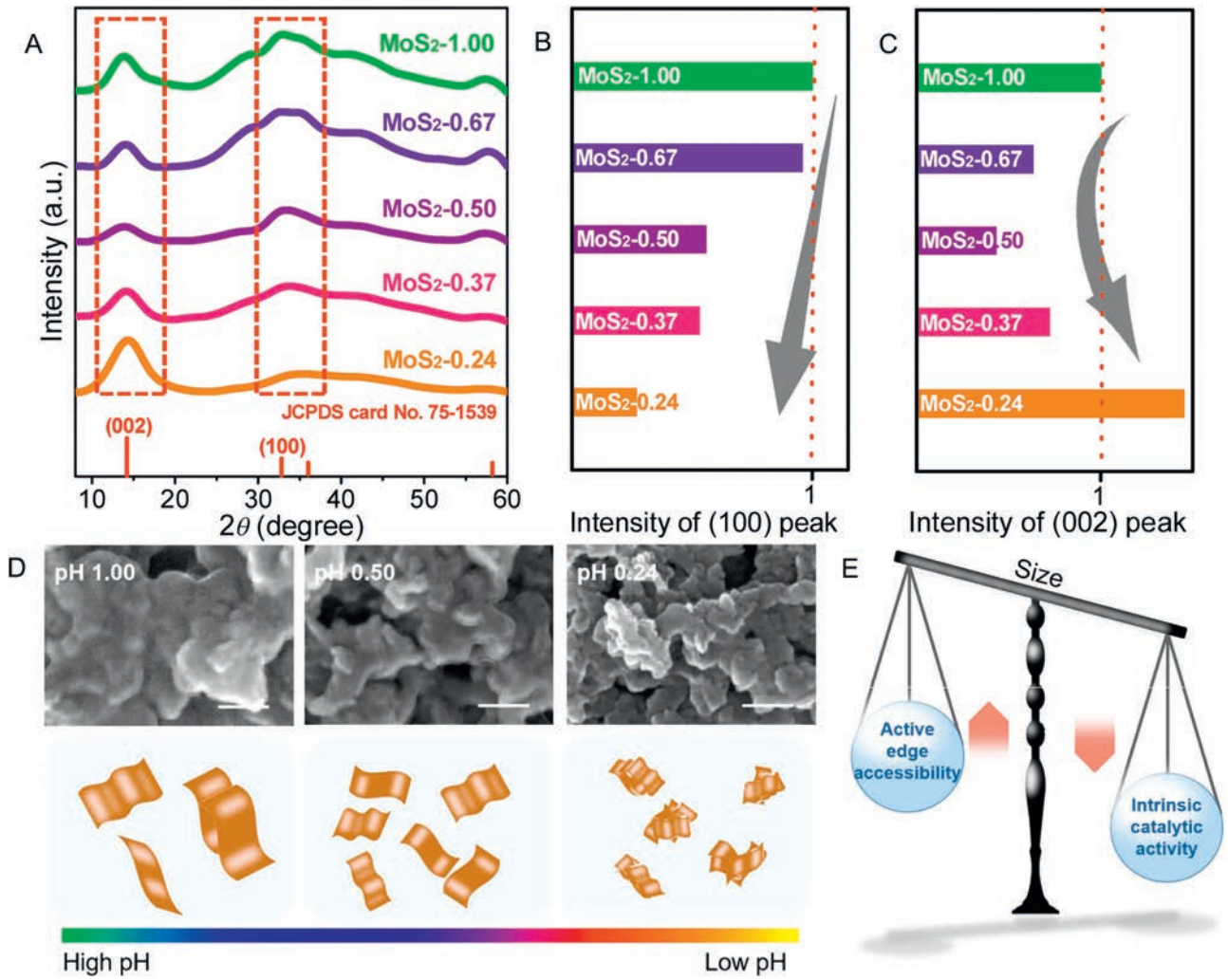

Fig. 1. (A) XRD profiles of the MoS_2 synthesized with different pH. (B) Normalized XRD intensity of (002) peak and (C) (100) peak. (D) SEM images (scale bar: 100 nm) and schematics of the effect of pH regulation on the resultant MoS_2. (E) Schematics of the trade-off between the intrinsic catalytic activity and the active edge accessibility determined by nanosheets size.

intrinsic activity, but the resultant restacking with narrow d-spacing between neighboring sheets is harmful for the exposition of active sites (Fig. 1E). Therefore, the size of MoS_2 nanosheets should be optimized.

After having demonstrated the particle size was determined by various pH values from characterization in Fig. 1, we tried to address the synthesis process of proton-induced MoS_2 that is schematically shown in Fig. 2A. When dissolved in HCl solution, the MoO_4^{2-} can be condensed into polymolybdate groups by protonation as following reactions (1), (2) simultaneously [37]:

$$7MoO_4^{2-} + 8H^+ \rightarrow Mo_7O_{24}^{6-} + 4H_2O \quad (1)$$

$$8MoO_4^{2-} + 12H^+ \rightarrow Mo_8O_{26}^{4-} + 6H_2O \quad (2)$$

Compared with the MoO_4^{2-}, the as-formed polymolybdate groups are more reactive and can be reduced by thiourea even under normal temperature and pressure, indicated by a vivid color change, in sharp contrast with that without proton pre-treatment (Fig. 2A and Fig. S1). These polymolybdate groups may serve as nucleation sites for the subsequent fast hydrothermal reaction. Consequently, the reaction time was greatly shortened from 20 h to 3 h assisted by the pre-formation of polymolybdate groups. As schematically shown in Fig. 2B, we further proposed the following mechanism for this pH regulation effect. At high pH (*e.g.*, pH 1.00), less polymolybdate groups are formed to play the role of nucleation active centers, so more Mo sources participate in the crystal growth process, which results in the formation of large-sized MoS_2 sheets; at low pH (*e.g.*, pH 0.24), more polymolybdate groups are formed, leading to the formation of the small-sized MoS_2 nanosheets. Since the smaller nanosheets suffer from a restacking problem, which is unfavorable to edges exposure and the catalytic performance on the electrode level.

We further investigated the electrocatalytic performance of these drop-casted size-controlled MoS_2 *via* a standard three-electrode setup with 0.5 mol/L H_2SO_4 as the electrolyte. The electrochemical measurements were carried out with a constant mass loading of 0.21 mg/cm^2 of MoS_2 catalysts on the glassy carbon electrode and carbon paper (Fig. S4 in Supporting information), and the effects of substrate on the final activity of MoS_2 catalysts can be ignored. As shown in Fig. 3A, among the three MoS_2 species, the one synthesized under the medium pH of 0.50 exhibits the best performance, delivering the lowest overpotential (η ~200 mV) at the current density of 10 mA/cm^2. Corresponding Tafel plots of the three MoS_2 samples also show the same tendency (Fig. 3B). The Tafel slope decreases from 83.3 mV/dec (MoS_2-1.00) to 46.3 mV/dec (MoS_2-0.50) and then increase to 77 mV/dec (MoS_2-0.24). The Tafel slope of MoS_2-0.50 suggests that they match the

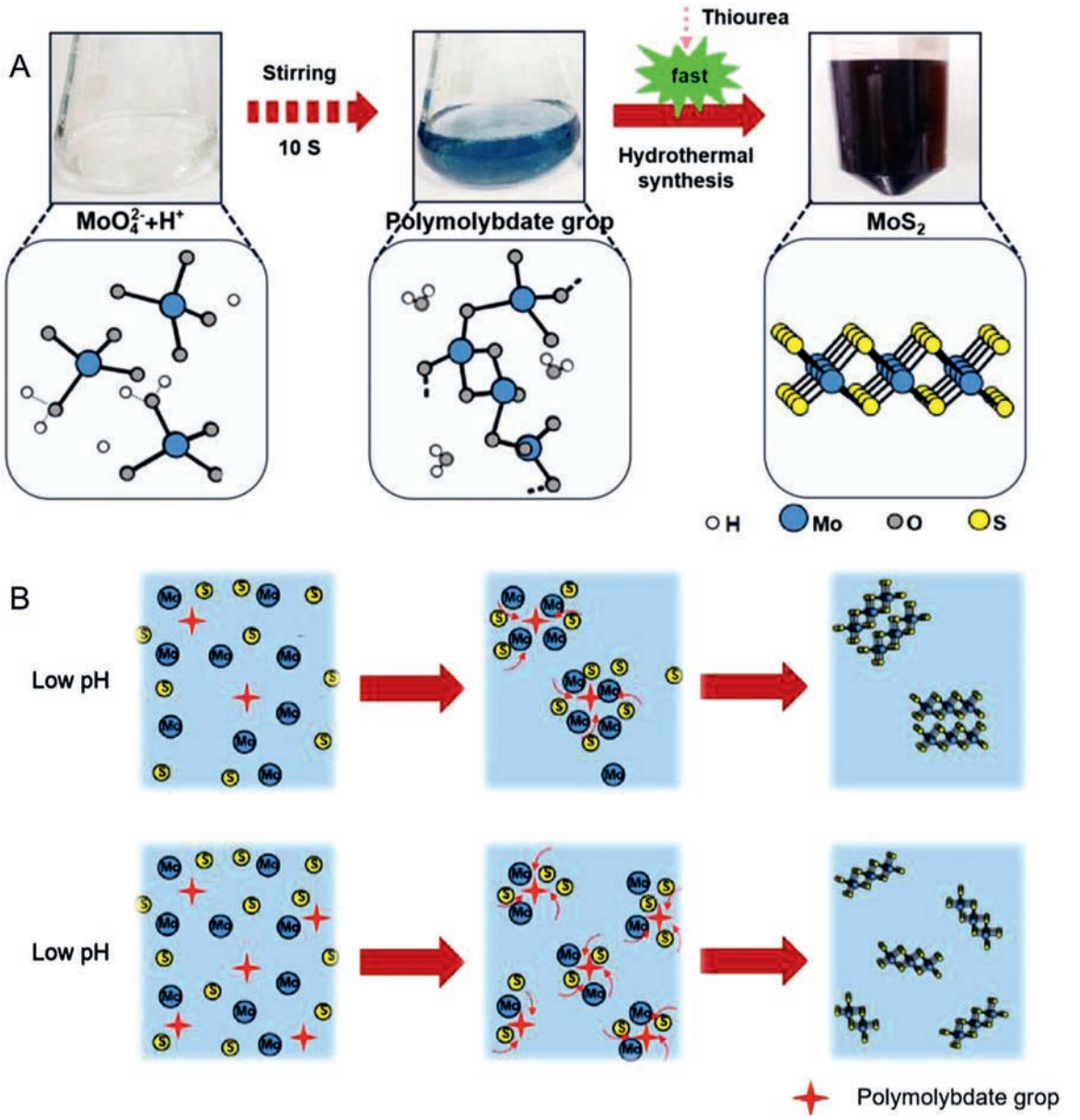

Fig. 2. (A) Process of the proton-induced fast synthesis process of MoS_2 nanocatalysts, (top) optical photos showing the color change of the reaction system at successive steps and (bottom) schematics of the species in the reaction systems. (B) Schematic illustration of the reaction process of MoS_2 with different pH pre-treatments.

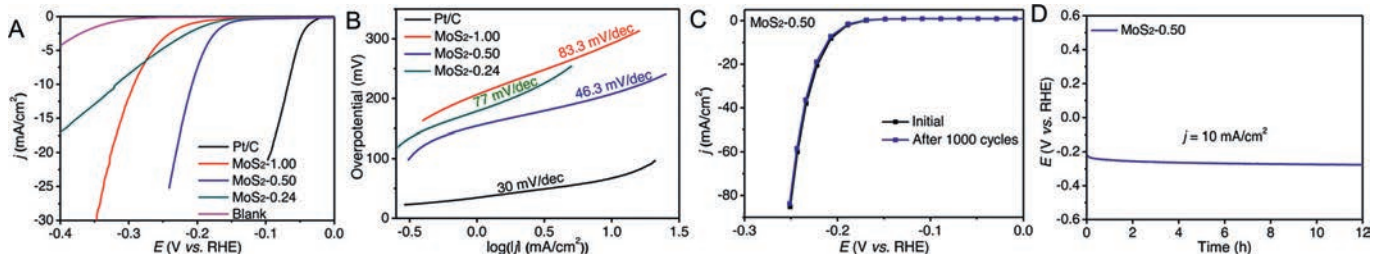

Fig. 3. Characterizations on the electrocatalytic performance of the synthesized size-controllable MoS_2 on the glassy carbon electrode. (A) LSV plots. (B) Tafel plots. The long-term electrochemical stability of the MoS_2 synthesized with pre-treatment of pH 0.50: (C) CV curves and (D) chronopotentiometry plot at a constant current density of 10 mA/cm^2.

Volmer-Heyrovsky mechanism. The electrocatalytic performance of MoS_2-0.50 is compatible with recent notable works (Table S2 in Supporting information).

Notably, the catalytic performances of the three kinds of MoS_2 are well consistent with their intensity of (002) peaks in the XRD profiles (Fig. 1C). These demonstrate that MoS_2-1.00 with larger and thicker nanosheets and MoS_2-0.24 with serious restacking show a compromised HER performance. Furthermore, the long-term electrochemical stability of MoS_2-0.50 is also examined by CV and chronopotentiometry scan (at 10 mA/cm^2). As shown in

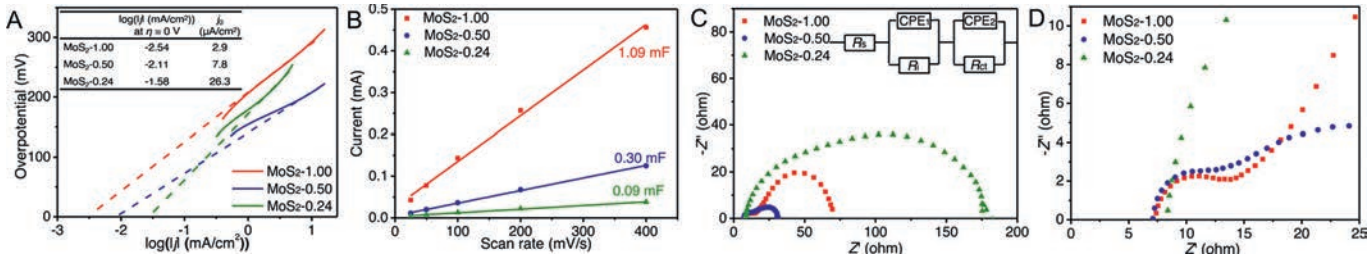

Fig. 4. Evaluations on the electrochemical characteristics of the synthesized MoS_2 on the glassy carbon electrode. (A) Calculated exchange current densities by applying the extrapolation method to the Tafel plots. (B) The derived C_{dl} under different scan rates. (C, D) Nyquist plots and (D) is the magnified high frequency region.

Fig. 3C, MoS_2-0.50 affords a similar CV curve after 1000 cycles, and a negligible increase of overpotential can be observed under a constant current density of −10 mA/cm^2 for 12 h (Fig. 3D).

To further demonstrate the possible origins of such different performances of these size-controlled MoS_2, exchange current density (j_0), double layer capacitance (C_{dl}), and EIS were carried out. j_0 represents the inherent activity for HER, which is obtained by extrapolating E-I data to the Tafel equation [20]. It can be seen that the activity of the MoS_2 catalyst is improved along with the decrease of pH (from pH 1.00 to 0.24), demonstrated by the increase of j_0 from 2.9 μA/cm^2 (MoS_2-1.00) to 7.8 μA/cm^2 (MoS_2-0.50) and 26.3 μA/cm^2 (MoS_2-0.24) as shown in Fig. 4A. These results can be explained by the size of the three kinds of MoS_2 nanocatalysts. C_{dl} was carried out to evaluate the electrochemically active surface area (ECSA) of each sample [38,39]. As shown in Fig. 4B, the capacitive current corresponding to the measured CV curves (Fig. S5 in Supporting information) is plotted as the function of the scan rates, from which the C_{dl} is extracted to evaluate the ECSA. As can be seen, the C_{dl} decreases from 1.09 mF (MoS_2-1.00) to 0.09 mF (MoS_2-0.24), suggesting adsorbable sites decreases along with the decrease of pH during the synthesis process. Note that not all adsorbable sites can be used for hydrogen evolution. EIS was performed to examine the electrode kinetics. As shown in Fig. 4C, the two semicircles at the low and the high frequencies represent the charge transfer resistance (R_{ct}) and the non-negligible electronic resistance of MoS_2 (R_i), respectively [40]. The smaller R_{ct} and R_i can afford faster HER kinetics. Detailed data of R_{ct} and R_i are exhibited in Table S3 (Supporting information). The R_{ct} decreases from 54.1 Ω (MoS_2-1.00) to 22.3 Ω (MoS_2-0.50), and then increases to 131.6 Ω (MoS_2-0.24). The R_{ct} corresponds to their LSV performance and Tafel slopes. Notably, the R_i keeps increasing along with the decrease of pH, from 5.3 Ω (MoS_2-1.00) to 5.9 Ω (MoS_2-0.50) and 40.4 Ω (MoS_2-0.24) (Fig. 4D). This result can be attributed to the downsizing of MoS_2 nanosheets, which impairs the electron migration in the electrode.

From the above electrochemical characterizations, we summary the mechanism of the pH regulation as follows. The increase of proton concentrations can effectively decrease the size of MoS_2 nanosheets to produce more unsaturated sulfur, endowing an enhanced intrinsic catalytic activity of each nanosheet. However, the serious aggregation occurs in these highly-active small-sized nanosheets, which will impair the system conductivity and electrolyte-accessibility. That may be the reason for MoS_2-0.50, which holds moderate intrinsic activity and the restacking degree and delivers the best electrode performance among the three.

Importantly, we have shown that the small difference in the size of these MoS_2 products will lead to such diverse electrode-level performances. Much attention should be paid to catalytic electrode construction apart from the chemical structure of the catalysts.

In this work, we put forward a strategy to realize the fast synthesis method of size-controllable MoS_2 nanocatalysts. Through an additional pre-treatment by HCl, nanosized MoS_2 catalysts can be synthesized simply and controllably by the hydrothermal reaction that achieves a superior performance of electrocatalysts without dopant. We demonstrate that lowing pH value can effectively decrease the size of resultant MoS_2 nanosheets, which will increase the intrinsic catalytic activity but lead to the restacking problem. By adjusting the size of MoS_2 nanoparticle, an excellent HER performance can be exhibited with a small overpotential of ~200 mV at 10 mA/cm^2, a low Tafel slope of 46.3 mV/dec and long-time stability. These findings will encourage further studies on the engineering of the catalytic electrode construction apart from the intrinsic activity of catalyst to improve the catalytic performance. Moreover, the proton-induced fast hydrothermal reaction in 3 h provides a new pathway for the large-scale application of highly active MoS_2 catalysts.

Declaration of competing interest

The authors report no declarations of interest.

Acknowledgments

This work was supported by the National Natural Science Foundation of China (No. 21905206) and Shanghai Sail Program (No. 19YF1450800).

Appendix A. Supplementary data

Supplementary material related to this article can be found, in the online version, at doi:https://doi.org/10.1016/j.cclet.2020.08.005.

References

[1] M.S. Dresselhaus, I.L. Thomas, Nature 414 (2001) 332–337.
[2] Q. Liu, J. Tian, W. Cui, et al., Angew. Chem. Int. Ed. 53 (2014) 6710–6714.
[3] X. Shang, W. Hu, X. Li, et al., Electrochim. Acta 224 (2017) 25–31.
[4] X. Zou, Y. Zhang, Chem. Soc. Rev. 44 (2015) 5148–5180.
[5] Y. Zhang, G. Wang, J. Tao, et al., FlatChem 14 (2019) 100087.
[6] J. Li, C. Liu, J. Wei, et al., Chin. Chem. Lett. 32 (2021) 880–884.
[7] C. Sun, J. Zhang, J. Ma, et al., J. Mater. Chem. A 4 (2016) 11234–11238.
[8] C. Cui, R. Cheng, C. Zhang, X. Wang, Chin. Chem. Lett. 31 (2020) 988–991.
[9] J. Ryu, Y. Surendranath, J. Am. Chem. Soc. 141 (2019) 15524–15531.
[10] W. Chen, C. Wang, K. Sasaki, et al., Energy Environ. Sci. 6 (2013) 943–951.
[11] Y. Li, H. Wang, L. Xie, et al., J. Am. Chem. Soc. 133 (2011) 7296–7299.
[12] P. Xiao, M.A. Sk, L. Thia, et al., Energy Environ. Sci. 7 (2014) 2624–2629.
[13] H. Zhou, F. Yu, Y. Liu, et al., Energy Environ. Sci. 10 (2017) 1487–1492.
[14] F. Hu, S. Zhu, S. Chen, et al., Adv. Mater. 29 (2017) 1606570.
[15] J. Tao, Y. Zhang, S. Wang, et al., ACS Appl. Mater. Interfaces 11 (2019) 18342–18348.
[16] M. Acerce, D. Voiry, M. Chhowalla, Nat. Nanotechnol. 10 (2015) 313–318.
[17] C. Liu, X. Zhao, S. Wang, et al., ACS Appl. Energy Mater. 2 (2019) 4458–4463.
[18] W. Jaegermann, H. Tributsch, Prog. Surf. Sci. 29 (1988) 1–167.
[19] B. Hinnemann, P.G. Moses, J. Bonde, et al., J. Am. Chem. Soc. 127 (2005) 5308–5309.
[20] T.F. Jaramillo, K.P. Jørgensen, J. Bonde, et al., Science 317 (2007) 100–102.
[21] T. Guo, L. Wang, S. Sun, et al., Chin. Chem. Lett. 30 (2019) 1253–1260.
[22] X. Hai, K. Chang, H. Pang, et al., J. Am. Chem. Soc. 138 (2016) 14962–14969.
[23] X. Zhang, Z. Lai, C. Tan, H. Zhang, et al., Angew. Chem. Int. Ed. 55 (2016) 8816–8838.
[24] J. Xie, H. Zhang, S. Li, et al., Adv. Mater. 25 (2013) 5807–5813.
[25] H. Li, K. Yu, C. Li, et al., Sci. Rep. 5 (2015) 18730–18730.
[26] J. Lao, D. Li, C. Jiang, et al., Nanoscale 12 (2020) 10158–10165.

[27] S. Park, D.Y. Chung, D. Ko, et al., J. Mater. Chem. A 4 (2016) 12720–12725.
[28] P. Cheng, C. Yuan, Q. Zhou, et al., J. Phys. Chem. C 123 (2019) 5833–5839.
[29] Y. Luo, X. Li, X. Cai, et al., ACS Nano 12 (2018) 4565–4573.
[30] Z. Xiang, Z. Zhang, X. Xu, Q. Zhang, C. Yuan, Carbon 98 (2016) 84–89.
[31] Z. Zhang, W. Li, M.F. Yuen, et al., Nano Energy 18 (2015) 196–204.
[32] C. Han, Z. Tian, H. Dou, D. Wang, X. Yang, Chin. Chem. Lett. 29 (2018) 606–611.
[33] Y. Tang, Y. Wang, X. Wang, et al., Adv. Energy Mater. 6 (2016) 1600116.
[34] J. Xie, J. Zhang, S. Li, et al., J. Am. Chem. Soc. 135 (2013) 17881–17888.
[35] W. Hu, G. Han, F. Dai, et al., Int. J. Hydrogen Energy 41 (2016) 294–299.
[36] G. Wang, J. Tao, Y. Zhang, et al., ACS Appl. Mater. Interfaces 10 (2018) 25409–25414.
[37] C.V. Krishnan, M. Garnett, B. HsiaoInt, B. Chu, J. Electrochem. Sci. 2 (2007) 29–51.
[38] Z. Chen, M. Chen, X. Yan, et al., ACS Nano 14 (2020) 6968–6979.
[39] J. Kibsgaard, Z. Chen, B.N. Reinecke, et al., Nat. Mater. 11 (2012) 963–969.
[40] H. Vrubel, T. Moehl, M. Grätzel, X. Hu, Chem. Commun. 49 (2013) 8985–8987.